

# Northumbria Research Link

Citation: Chen, Wenge, Yang, Yixiao, Zhao, Qian, Liu, Xiaoteng and Fu, Yong Qing (2022) Nanoscale mechanics of metal-coated graphene nanocomposite powders. Materials Today Communications, 33. p. 104731. ISSN 2352-4928

Published by: Elsevier

URL: <https://doi.org/10.1016/j.mtcomm.2022.104731>  
<<https://doi.org/10.1016/j.mtcomm.2022.104731>>

This version was downloaded from Northumbria Research Link:  
<https://nrl.northumbria.ac.uk/id/eprint/50908/>

Northumbria University has developed Northumbria Research Link (NRL) to enable users to access the University's research output. Copyright © and moral rights for items on NRL are retained by the individual author(s) and/or other copyright owners. Single copies of full items can be reproduced, displayed or performed, and given to third parties in any format or medium for personal research or study, educational, or not-for-profit purposes without prior permission or charge, provided the authors, title and full bibliographic details are given, as well as a hyperlink and/or URL to the original metadata page. The content must not be changed in any way. Full items must not be sold commercially in any format or medium without formal permission of the copyright holder. The full policy is available online: <http://nrl.northumbria.ac.uk/policies.html>

This document may differ from the final, published version of the research and has been made available online in accordance with publisher policies. To read and/or cite from the published version of the research, please visit the publisher's website (a subscription may be required.)



**Northumbria  
University**  
NEWCASTLE



**UniversityLibrary**

# Nanoscale Mechanics of Metal-coated Graphene Nanocomposite Powders

Wenge Chen <sup>a\*</sup>, Yixiao Yang <sup>a</sup>, Qian Zhao <sup>a</sup>, Xiaoteng Liu <sup>b</sup>, Yong-Qing Fu<sup>b\*</sup>

<sup>a</sup> School of Materials Science and Engineering, Xi'an University of Technology,  
Xi'an, Shaanxi, 710048, P.R. China

<sup>b</sup> Faculty of Engineering and Environment, Northumbria University, Newcastle upon  
Tyne, NE1 8ST, UK.

## Abstract

Nanoscale mechanical properties of graphene and metal-coated graphene nanocomposite powders were evaluated using a nano-indentation method with an atomic force microscope. The obtained results were then verified using the data obtained from the first principle calculations. Graphene synthesized using the modified Hummer method showed a layered structure with a thickness of ~1.1 nm. Metal coated graphene nanocomposite powders, including copper-coated graphene ones (Cu@graphene) and nickel-coated graphene ones (Ni@graphene), were synthesized using an *in-situ* co-reduction method. The obtained average values of Young's moduli of graphene, Cu@graphene and Ni@graphene from the nano-indentation tests were 0.98 TPa, 1.03 TPa and 1.06 TPa, and their moduli obtained using the first principle calculations were 1.051 TPa, 1.07 TPa, and 1.10 TPa, respectively. The calculated binding energy values between metal and graphene were -1.54 eV for Cu@graphene and -3.85 eV for Ni@graphene. Significant charge transfers between carbon atoms and metal atoms were found to apparently enhance the bond strengths of both C-C and metallic bonds.

**Keywords:** Graphene; metal@graphene; mechanical properties; nano-indentation; first-principles calculation

---

<sup>1</sup> Corresponding authors: Professor Wenge Chen; Professor Richard Y.Q.Fu.

E-mail: [wgchen001@263.net](mailto:wgchen001@263.net) (W.G. Chen), [richard.fu@northumbria.ac.uk](mailto:richard.fu@northumbria.ac.uk) (Richard Y.Q. Fu)

## 1. Introduction

Graphene is a two-dimensional carbon nanomaterial with a honeycomb-like crystal structure, composed of carbon atoms and  $sp^2$  hybrid orbitals<sup>[1]</sup>, and has excellent electrical, optical, thermal and mechanical properties. It is one of the materials with extremely high strengths, and its theoretical Young's modulus and intrinsic strength can be as high as  $\sim 1.1$  TPa and  $\sim 130$  GPa.<sup>[2]</sup> These unique properties make graphene having wide-range application prospects in various fields such as supercapacitors, fuel cells, sensors, and nanocomposites.<sup>[3]</sup>

Due to its unique two-dimensional nature, advanced mechanical techniques such as atomic force microscope (AFM) or nanoindentation are frequently used to characterize its mechanical properties. For example, Lee et al.<sup>[2]</sup> deposited graphene on the surface of a Si membrane, and characterized the relationship between applied load and indentation depth using an AFM based nanoindentation technology. Their obtained Young's modulus of graphene was  $1.0 \pm 0.1$  TPa and its intrinsic strength was  $130 \pm 10$  GPa<sup>[2]</sup>.

For theoretical analysis and numerical simulations, most researchers studied mechanical properties of graphene based on continuum theories<sup>[4-6]</sup>. For example, Shokrieh et al.<sup>[4]</sup> predicted Young's modulus of graphene sheets to be 1.04 TPa using a continuous mechanics method. Liu et al.<sup>[5]</sup> calculated Young's modulus and Poisson's ratio of graphene to be 1.05 TPa and 0.186 using the first principle calculation method. Meo et al.<sup>[6]</sup> simulated mechanical characteristics of graphene under the unidirectional tension based on finite element analysis, and predicted that its average Young's modulus was 0.95 TPa.

Recently graphene-based nanocomposites and their mechanical properties have become a popular research topic for both academia and industry. For example, Giannopoulos et al.<sup>[7]</sup> investigated mechanical behavior of epoxy-reinforced graphene nanocomposites using a multi-scale structural mechanics approach and predicted that the Young's modulus of the composite was 0.738 TPa and the Poisson's ratio was 0.474. Spanos et al.<sup>[8]</sup> used a finite element method to simulate mechanical properties of a

graphene-based composite and showed that its mechanical properties are dependent on the size of graphene sheets.

When graphene is used in the composite materials, there are potential problems such as severe agglomeration, poor wettability of graphene with certain metallic materials and poor interfacial bonding between them. For this reason, nanocomposites such as metal coated graphene (i.e., metal@graphene) were synthesized using various chemical or physical processes [9-11]. Using these advanced synthesis methods, the composites not only maintain excellent catalytic, photoelectric and magnetic properties of metal or graphene, but also show less agglomeration of graphene and metal powders. Therefore, they have great potentials for applications in energy, catalysis and biology [12-15].

At present, there are many reports on first-principles studies of graphene, which are mainly focused on its electronic structure, phonon spectrum, and optical or other functional properties. For example, Sun et al.<sup>[16]</sup> investigated C-H and F-C hydrogen bonds in graphene/fluorographene through first-principles calculations. Mullen et al.<sup>[17]</sup> calculated the band structures of graphene. Their results showed that the conduction band and valence band of graphene are intersected at the Fermi level, which indicates that the graphene's band gap is zero, and the single layer graphene is metallic. Vandenberghe et al.<sup>[18]</sup> calculated the density of states of graphene. They showed that for the total density of states of graphene, 2p electrons have two obvious peaks at energies of -6.200 eV and 8.639 eV, whereas 2s electrons have no obvious peaks at these values. This indicates that the distribution of total density of states is mainly contributed by the 2p electrons of graphene. Ji et al.<sup>[19]</sup> investigated double-side contact performance of the catalyst metal and graphene using the first-principle calculation, and showed that two catalytic metals of Pt and Ir have extremely small contact resistances in the double-side contact (DSC). At the same time, these two metals show chemical adsorption characteristics in the DSC, because the  $d_z^2$  orbital of Pt interacts with the  $p_z$ -orbital of graphene and the interfacial electronic structure are altered by a charge redistribution. Wang et al.<sup>[20]</sup> used the density functional theory and calculated structures and electronic properties of van der Waals (vdWs) heterostructures formed by graphene and graphene-like germanium carbides. They found that the Schottky

barrier in the graphene can be effectively tuned by changing the interlayer distances in the vdW heterostructures. Kim et al. <sup>[21]</sup> showed that ultra-high strength vanadium (V)-graphene nanolayers have a good radiation resistance, and reported that the radiation hardening rate of the V-graphene nanoparticles before and after irradiation was significantly reduced with the addition of a graphene layer. Drost et al. <sup>[22]</sup> investigated graphene-BN interfaces with a length of 150 nm or more, and found that C-B and C-N interface energies were 0.03 eV and 0.9 eV, respectively. Zhang et al. <sup>[23]</sup> conducted first-principle calculations of the electronic and mechanical properties of graphene/Cu composites, and showed that their Young's moduli, shear moduli and bulk moduli were increased up to 149%, 156%, and 108%, respectively, compared with those of pure copper. All these studies show that graphene effectively enhances the strength of the metal matrix composites.

For the metal@graphene composites, Hu et al. <sup>[24]</sup> used first-principles density functional theory and generalized gradient approximation to study the adsorption behavior of 15 different transition metal atoms coated onto graphene, and calculated their adsorption energy, stable geometric configuration, density of states, magnetic moment. Sun et al. <sup>[25]</sup> used first-principles calculations and studied geometric structures, electronic structures and magnetic properties of alkaline earth metal atoms adsorbed on the graphene. They reported that some atoms such as Ca, Sr, and Ba are adsorbed on graphene by forming strong ionic bonds with graphene, which causes the changes in the graphene's electronic and magnetic properties. Zhou et al. <sup>[26]</sup> used density functional theory to study energy, electron and magnetism of transition metal atoms modified graphene, including boron doping, vacancies and the combination of these two. Sun et al. <sup>[27]</sup> investigated electronic structures and magnetic behaviors of graphene substituted with transition metal atoms through the first-principles calculations. Their results show that substitutions of La and Ta elements make the graphene showing metallic properties, whereas substitutions of Hf, Os and Pt elements make the graphene showing semiconducting properties. Chi <sup>[28]</sup> et al. studied adsorption behavior of formaldehyde on intrinsic and aluminum-doped graphene sheets using the density functional theory. Jiang et al. <sup>[29]</sup> used first-principle method based on the density functional theory to study optoelectronic properties of pure graphene, nitrogen-doped graphene, gallium-doped graphene, and nitrogen-gallium co-doped graphene. These studies proved that the metal@graphene composites have excellent electrical and

mechanical properties.

Although there are many studies on mechanical, electrical and physical properties of graphene and graphene composites, as far as we know, there are few studies on the nanoscale mechanical properties of metal@graphene nanocomposite powders, and few studies have explored microscopic mechanisms, charge transfer, and interaction forces between the metal atom and graphene in the nanocomposites. Therefore, the main objective of this study is to explore a suitable experimental method to precisely evaluate the Young's moduli and mechanical properties of Cu and Ni coated graphene nanopowders. The obtained results are verified by first-principles calculations based on their band structures and binding energies.

## 2. Materials and Methods

### 2.1. Material preparation and characterization

The raw materials used in this study were flakes of high-purity graphite powders (with an average size of  $\sim 74\ \mu\text{m}$ , 99.90% purity, purchased from Nanjing Xian Feng Nano Materials Technology Co. Ltd., Jiangsu, China). Graphite oxides (GO) were obtained from the commercial graphite using a modified Hummer method<sup>[30]</sup>. The GO was reduced into rGO using an ascorbic acid through a chemical reduction<sup>[31]</sup>.

The GO was applied to fabricate metal@graphene nanocomposite powders using an *in-situ* co-reduction method. Cu and Ni were synthesized onto graphene using a thermo-electroless plating method.<sup>[28]</sup> The GO suspension was added into the electroless plating solution, which was composed of  $\text{CuSO}_4$  or  $\text{NiSO}_4$ , ascorbic acid and polyvinylpyrrolidone. The Cu plating was stirred for 3 hours at  $90^\circ\text{C}$  and nickel plating was lasted for 0.5 hours at  $30^\circ\text{C}$ , with the pH values of the solutions adjusted to 9 to 11. More details about this process can be found in Ref.<sup>[32]</sup>

Crystalline structures of graphene and metal@graphene nanocomposite powders were analyzed using an X-ray diffractometer (XRD-7000S, Shimadzu, Japan) with  $\text{Cu K}\alpha$  radiation operated at 40 kV and 15 mA. The scanning range of  $2\theta$  angles was from  $15$  to  $85^\circ$  and the scanning speed was  $2^\circ/\text{min}$ . The samples were also characterized using a Raman spectrometer (Via Reflex, Renishaw, London, UK) with a laser

wavelength of 532 nm and a scanned range over 500-3500 cm<sup>-1</sup>. All the Raman spectra were taken at room temperature (20°C). Microstructures of the obtained powders were analyzed using a transmission electron microscope (TEM, JEM-3010, JEOL, Akishima-shi, Japan) and a scanning electron microscope (SEM, TESCAN VEGA3 XMU, TESCAN, Czech Republic). Thickness of the graphene and composites was characterized using a tapping mode AFM (Dimension FastScan, Bruker, Karlsruhe, Germany). During the measurement, a RTESPA-525 probe with a tip radius of 8 nm was used, and the scanning range of 3 × 3 μm<sup>2</sup> was selected. Multiple areas at different locations were scanned and the average thickness value was obtained. The gain of PID (i.e., proportion integral derivative) was adjusted to minimize the noise and improve the image quality. The resonance frequency used for the AFM tip was 300 kHz and the scanning speed was 1 Hz.

## 2.2. Determination of Young's modulus

Nanoscale mechanical properties were analyzed based on the force-distance curves obtained from AFM, which was operated in a Peak-Force tapping mode using the RTESPA-525 probe. When the AFM probe approached the sample, the microcantilever was gradually bent downward from its initial unloaded state due to the surface charge attraction of the sample. As the relative distance was gradually decreased, the attraction force exceeded the elastic force. Finally, the tip of the probe was directly contacted the surface of the sample. When the sample was continuously moved vertically upward, the microcantilever was bent upward due to the repulsion of the sample. At this moment, the probe tip was pressed into the sample and the surface of the sample was deformed.

Software of AtomicJ was used to convert the force-distance curves into force-indentation curves, and then the Young's modulus of the samples was obtained according to the Sneddon (conical) model <sup>[33]</sup>:

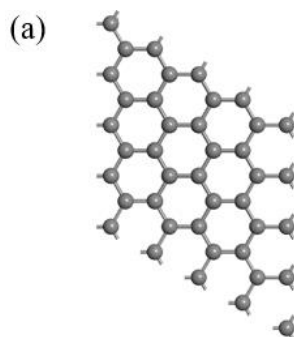
$$F = \frac{E}{1-\nu^2} \frac{2 \tan \alpha}{\pi} \delta^2 \quad (1)$$

where  $F$  is the applied load (nN),  $E$  is the Young's modulus (TPa),  $\nu$  is the Poisson's

ratio of the sample (0.3),  $\alpha$  is the tip half angle ( $25^\circ$ ), and  $\delta$  is the depth of indentation (nm). The fitting was required for calibration parameters, including the spring constant of the probe (116 N/m), the tip radius (8 nm) and the deflection sensitivity (86.7 nm/V).

### 2.3. Theoretical Analysis

To verify the measured mechanical properties, the first principles calculations were applied for comparisons. The graphene's model and the interface model of metal-coated graphene were firstly established. Figure 1 shows the model structure of graphene, which considers the periodic arrangement of crystal lattice with a vacuum layer of 20 Å in the Z direction, to eliminate the interactions between adjacent layers. Copper and nickel coated graphene samples have the highest intensity of diffraction peaks on their (111) crystal planes based on the XRD results. Therefore, this study builds models of (111)/graphene interfaces using three different building methods (e.g., Top, Hollow, Bridge) as shown in Figure 1. The Top position means that the metal atoms are located directly above the C atoms. The Hollow position means that the metal atoms are located above the centers of the carbon hexagon structures. The Bridge position means that the metal atoms are located above the middle positions of the C-C bonds. It is assumed no strong bonding between metal atoms and carbon atoms, therefore, the distance between them is the sum of the *van der Waals* gaps of two atoms<sup>[34]</sup>. We firstly set the distances between the Cu atomic plane and graphene, as well as Ni atomic plane and graphene to be 3.1 Å and 3.03 Å, respectively, and then the program relaxes the Ni@graphene distance to 3.33 Å during the following calculation process.





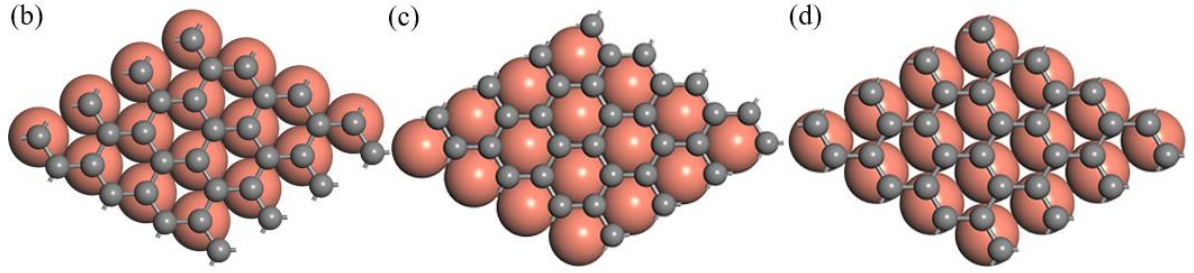


**Fig. 1.** The three models of (a) graphene, (b) (111)/graphene Top, (c) (111)/graphene Hollow, (d) (111)/graphene Bridge.

Three-dimensional periodic boundary conditions were applied in the calculations. To reduce the plane wave base of the electronic system, a plane wave ultrasoft pseudopotential (USP) was used to approximately describe the interactions between the valence electron and the ionic substance. Generalized Gradient Approximation (GGA) exchange correlation energy function was chosen for the exchange correlation energy. The Perdew Burke Ernzerhof (PBE) functional was used in the generalized gradient approximation, and the Broyden-Fletcher-Goldfarb-Shanno scheme (BFGS) algorithm was used for the structure optimization <sup>[35]</sup>. For achieving the convergence, the cut-off energies of graphene and metal-coated graphene were chosen as 450 eV and 500 eV, respectively, and the K points were  $5 \times 5 \times 1$  and  $6 \times 6 \times 2$ , respectively.

### 3. Results and Discussion

#### 3.1. Experimental results

SEM images of graphene (Figure 2(a)) and Ni/graphene composite powders (Figure 2(b)) show clearly that a thin metal layer is wrapped onto the graphene sheet (Figure 2(b)) in the composite powders. Figure 3 shows TEM images of graphene and metal@graphene nanocomposite powders. Graphene (Figure 3(a)) shows a tulle-like sheet structure with apparent wrinkles. This is because a two-dimensional material such as graphene easily forms wrinkles to become thermodynamically stable<sup>[36, 37]</sup>. The TEM image of Cu@graphene (Figure 3(b)) shows that fine copper particles are evenly distributed on the surfaces of graphene, and the size of the copper particles is about 10 nm. The TEM image of Ni@graphene (Figure 3(c)) shows that the size of nickel particles is about 30 nm, and its agglomeration is more obvious than that of

Cu@graphene. This is because nickel is easily magnetized. In the powder evaporation process using the air-blast drying, the large surface tension of the gas-liquid interfaces makes the powder agglomerated significantly.

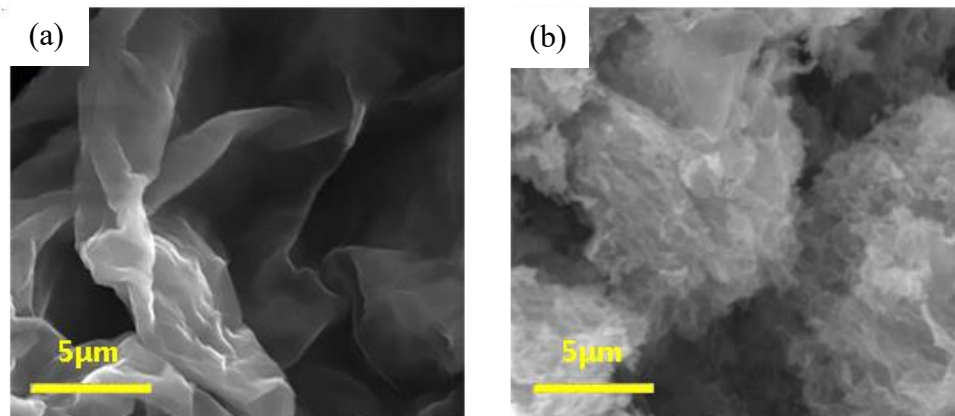


**Fig. 2.** SEM images showing the surface morphologies of (a) graphene, (b) Ni@graphene,

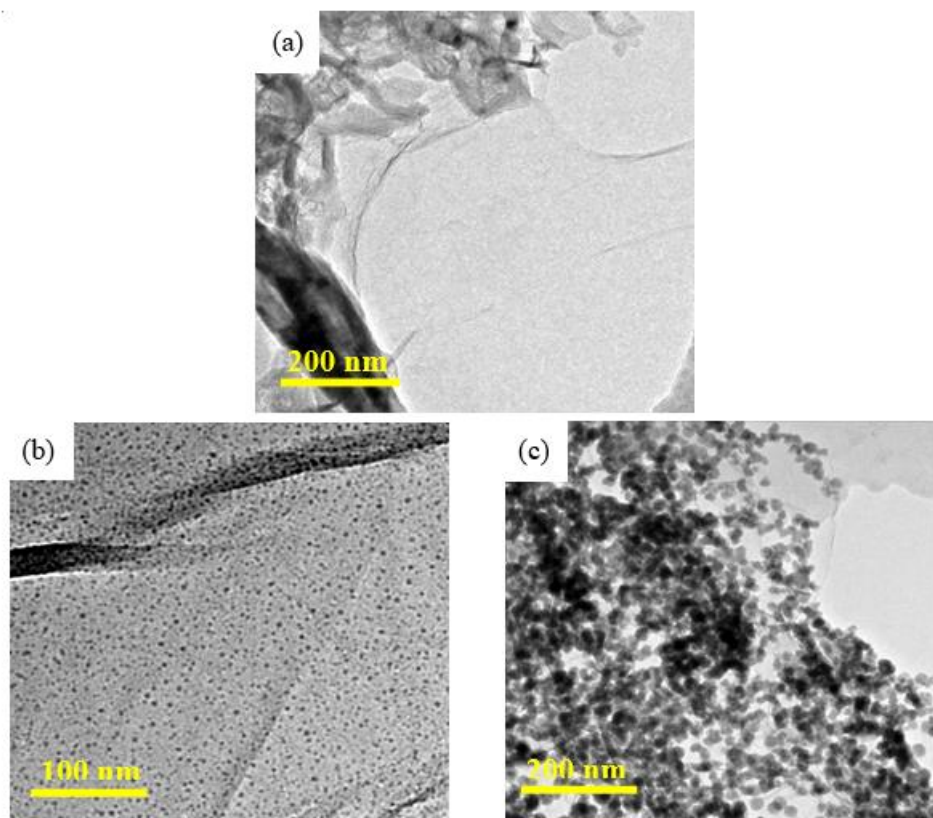


**Fig. 3.** TEM images of (a) graphene, (b) Cu@graphene, (c) Ni@graphene.

Figure 4 shows XRD patterns of graphene and metal@graphene nanocomposite powders. It can be seen that graphene (Figure 4(a)) has a distinct carbon characteristic peak at  $2\theta=26^{\circ}$ <sup>[38]</sup>. For the XRD result of Cu@graphene powder (Figure 4(b)), the C

diffraction peak is the same as that of graphene, indicating that GO has been reduced into graphene. There are also two peaks at  $43.3^\circ$  and  $50.4^\circ$  as shown in Figure 4(b), corresponding to (111) and (200) peaks of face-centered cubic Cu crystals. The crystallinity values of the graphene and composite powders are  $\sim 87.90\%$  and  $\sim 94.92\%$ , which were calculated using the Jade software (see Appendix). The peak of  $\text{Cu}_2\text{O}$  as the crystal impurity appears in Figure 4(b). This  $\text{Cu}_2\text{O}$  is generated during the chemical process, as also reported by Guo et al. [39]

For Ni@graphene (Figure 4(c)), no sharp peak is observed around  $2\theta = 26^\circ$  because the graphene surface is covered by Ni. A broad peak can be observed at  $2\theta = 44.9^\circ$  corresponding to that of Ni (111). The crystallinity was calculated to be  $\sim 4.13\%$  using the Jade software. This indicates that the crystallinity of Ni is very poor, which is quite different from the report from Cao et al [40]. Result indicates that the reaction and drying temperatures during the preparation process are probably not high enough as the temperature at which Ni can be converted from amorphous to crystalline is usually higher than 700 K [41].

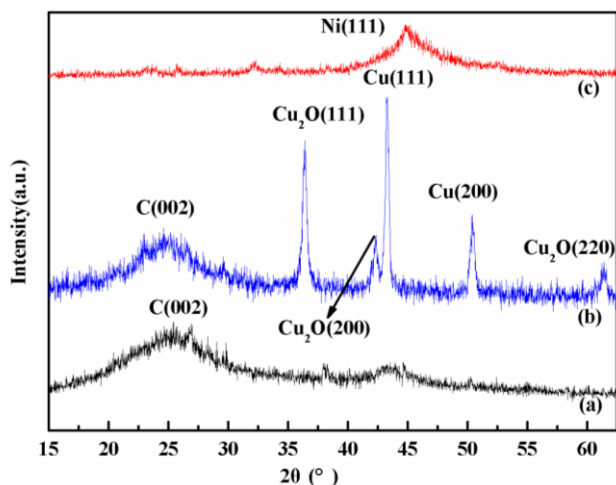


**Fig. 4.** XRD diagrams of (a) graphene, (b) Cu@graphene, (c) Ni@ graphene.

Figure 5 shows Raman spectra of graphene powders and metal@graphene nanocomposite powders. Three characteristic peaks can be seen from the Raman spectrum of graphene (Figure 5(a)), corresponding to the peaks of D, G and 2D. The D peak at  $1351\text{ cm}^{-1}$  is caused by two-phonon's second-order Raman resonance which is linked to crystal defects of carbon atoms [42]. Its intensity is proportional to the degree

of defect in graphene. The G peak at  $\sim 1598 \text{ cm}^{-1}$  is caused by monophonic first-order Raman resonance<sup>[43]</sup>, which is linked to the symmetry and structural order of materials. Its strength is proportional to the thickness of the graphene layer when the number of graphene layers is small. The 2D peak at  $\sim 2678 \text{ cm}^{-1}$  is caused by the double-phonon second-order Raman resonance, which shows the stacking of carbon atoms. Its intensity reflects the layer number information of graphene<sup>[44]</sup>. The intensity ratio of the D peak to the G peak ( $I_D/I_G$ ) in the Raman spectrum of the graphene powder (Figure 5(a)) is 1.056. The value of  $I_D/I_G$  for the Cu@graphene powder (Figure 5(b)) is 1.076, and that of  $I_D/I_G$  for the Ni@graphene (Figure 5(c)) is 1.104. The  $I_D/I_G$  ratios of Cu@graphene and Ni@graphene are similar to that of the graphene, which shows that Cu@graphene and Ni@graphene have been successfully obtained, similar to those reported by Dong et al<sup>[45]</sup>. When the D peak is very weak, it means that there are fewer defects in the prepared graphene<sup>[46]</sup>.

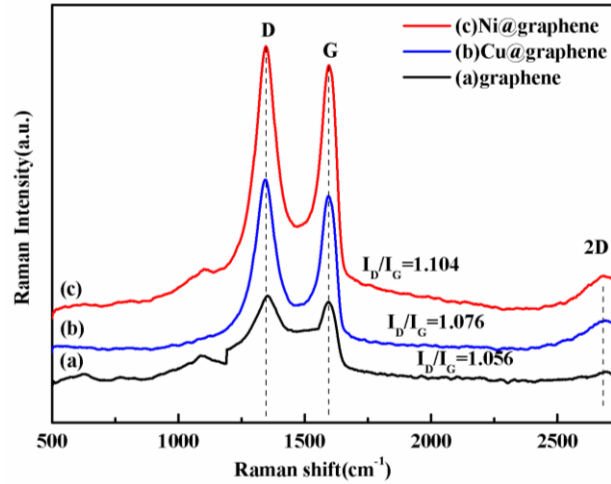


**Fig. 5.** Raman spectra of (a) graphene, (b) Cu@graphene, (c) Ni@ graphene.

Figure 6 shows AFM images of graphene and metal@graphene nanocomposite powders. The average thickness of a single-layer graphene is  $\sim 0.34 \text{ nm}$ , while the thickness of graphene in this study was measured to be  $0.7\text{-}1.2 \text{ nm}$  using the AFM. This variation is mainly due to the deviation of the measured thickness caused by the *van der Waals* radius of carbon and the adsorbents on the surface. As the number of graphene layers is increased, the thickness of graphene increases at a rate of  $0.34 \text{ nm/layer}$ <sup>[47]</sup>. It can be seen that graphene (Figure 6(a)) layer has a thickness of  $\sim 1.1$

nm, which is consistent with the results reported by Yao et al. <sup>[48]</sup> The thicknesses of Cu@graphene and Ni@graphene powders are increased due to the additions of copper and nickel particles on the surface: e.g., the thickness of the Cu@graphene (Figure 6(b)) is ~3.0 nm, whereas that of Ni@graphene (Figure 6(c)) is ~5.8 nm. The sizes of copper particles and nickel particles (Figure 6(b,c)) measured using the NanoScope Analysis software are ~9.93 nm and 31.619 nm, which are consistent with the results of TEM. The difference between the thickness measurement and the particle size measurement is probably because of the differences in measurement directions. On the other hand, because nanosized powders are easy agglomerated, the measured size of metal particle may be larger than the actual size of nano particle.

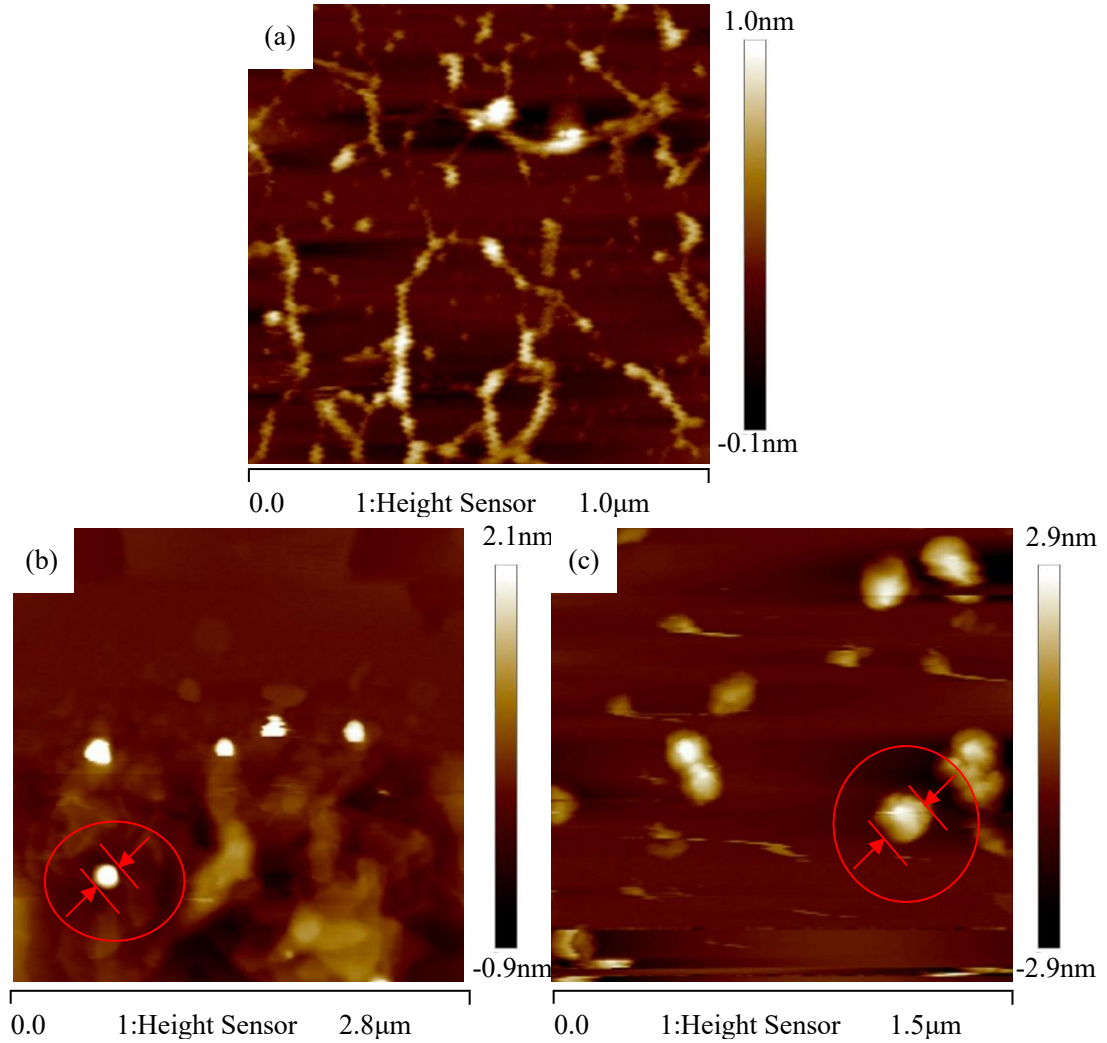


**Fig. 6.** AFM images of (a) graphene, (b) Cu@graphene, (c) Ni@graphene.

Figure 7 shows the force-distance curves measured using the Peak-Force Tapping

mode of AFM. The attached figure in Figure 7 is the nanoindentation map. For the graphene (Figure 7(a)), when the tip approaches the surface of the sample, the curve shows a zig-zag form. As the probe is continuously approach the sample, a turning point appears, which indicates that the tip has truly contacted the sample. According to the contact distance, the indented depth in graphene is estimated about 1.51 nm. The corresponding force at this point is ~106 nN. The indented depth in the Cu@ graphene (figure 7(b)) is about 2.98 nm, corresponding to a force of 170 nN. Whereas the indented depth into Ni@graphene (figure 7(c)) is about 5.65 nm, and the corresponding force is 480 nN. These indented depths are similar to the thicknesses of the samples. With the increase of indented depth, the applied force is increased. The force-displacement curves during the loading processes are all linear, which indicates that the samples all show elastic deformation. These curves are similar to those obtained from the standard compressive load-displacement curves. They reflect the linear interatomic displacements of the material under the action of an external force.



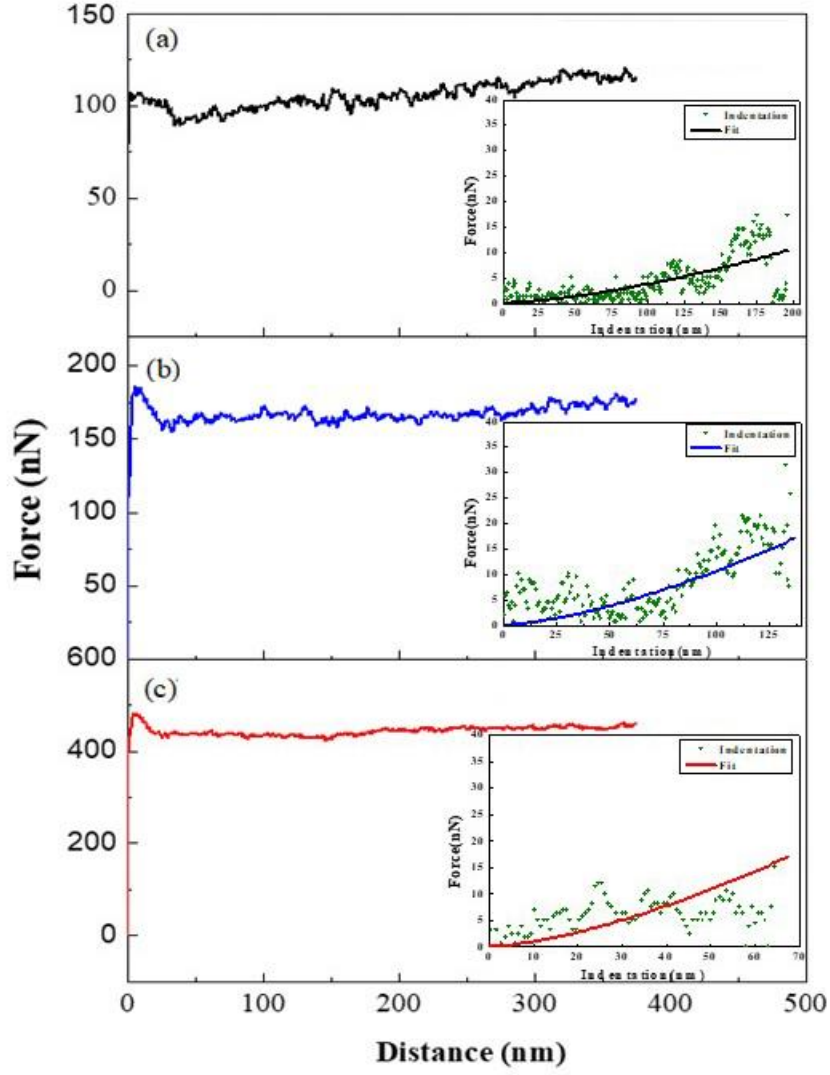


**Fig. 7.** Force-Distance curves and Force-Indentation curves of (a) graphene, (b) Cu@graphene, (c) Ni@graphene.

Figure 8 shows the corresponding force-indentation curves fitted by AtomicJ software according to the Sneddon (conical) model<sup>[49]</sup>. The curves are non-linear and the load is increased with the indentation depth. Each sample was tested five times and the obtained moduli are shown in Figure 8. The moduli were fitted by a Gaussian Function and the obtained average moduli of graphene (Figure 8(a)), Cu@graphene (Figure 8(b)) and Ni@ graphene (Figure 8(c)) are  $0.98 \pm 0.02$  TPa,  $1.03 \pm 0.03$  TPa and  $1.06 \pm 0.01$  TPa, respectively. The value of Young's modulus of graphene is similar to the result obtained from Lee et al. <sup>[2]</sup> The moduli of Cu@graphene and Ni@graphene do not show significant differences with that of graphene.

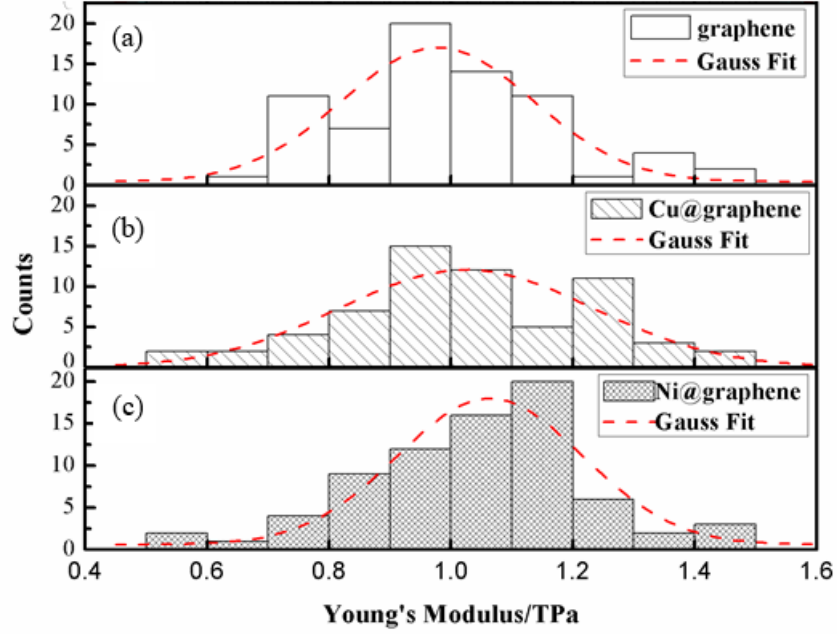


**Fig. 8.** Histogram and Gauss Fit of Young's moduli of (a) graphene, (b) Cu@graphene, (c) Ni@graphene.

### 3.2. Theoretical calculation results

Results of calculated energy bands and density of states for the graphene are shown in Figure 9, which are mainly used to verify our model. From the graphene energy band diagram (see Figure 9(a)), the conduction band and valence band of graphene are overlapping at the Fermi level, and the forbidden band width is 0.014 eV, close to zero. The results are consistent with the calculation results reported by Yang et al <sup>[31]</sup>. From the density of states diagram of graphene (see Figure 9(b)), there are two spikes on both sides of the Fermi level. The density of states diagram is V-shaped around  $E=0$ , and the density of states at the Fermi level is 0, which indicates that graphene is a zero-bandgap material. The density of states corresponding to the denser upper conduction band is the largest, with a value of 8.55 eV. Whereas the lower valence band is relatively sparse, corresponding to a small value of the density of states. All these simulation results prove that our simulation model is correct and can be used for the simulations of graphene composites.

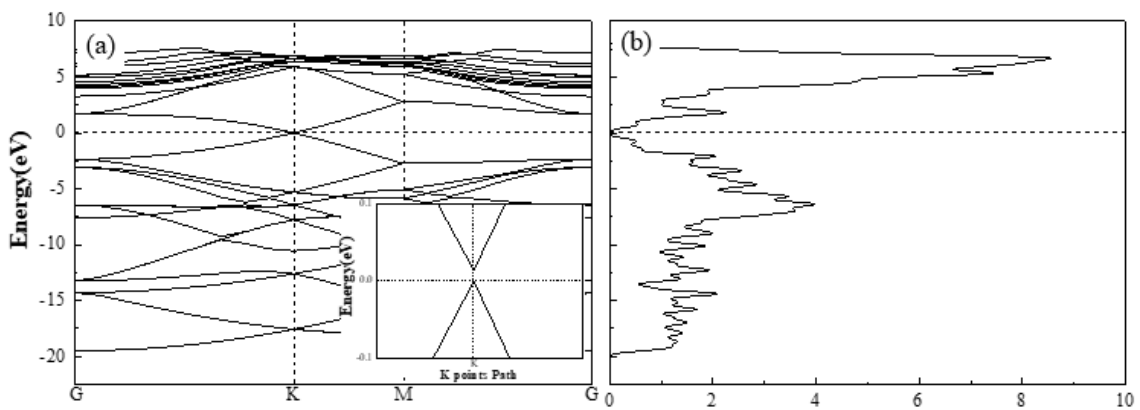




**Fig. 9.** (a) Band structure of graphene (the illustration is enlarged at Fermi level), and (b) density of states of graphene.

The closed path required for the calculation of the energy band structure and density of states of the Cu(111)/graphene interface model is the same as that of the graphene model. The obtained results are shown in Figure 10. Figures 10(a), 10(c), 10(e) are the energy band structure diagrams of Top position, Hollow position and Bridge position of Cu(111)/graphene, respectively. Compared with the energy band structure diagram of graphene, the Fermi levels of the Cu(111)/graphene samples are still at the intersection between the graphene  $\pi$  band and  $\pi^*$  band. Because a layer of copper atoms is built at the graphene interface, the conduction band passes through the Fermi level for the Cu@graphene sample. The forbidden band width is zero, indicating that the addition of copper into graphene does not change the zero bandgap characteristics of graphene. The result is consistent with the calculation results of Xu et al <sup>[50]</sup>.

For the energy band structure diagram of Cu@graphene interface model, the upper conduction band becomes less dense. On the contrary, the valence band near the Fermi level at the lower part is very dense, but it becomes sparse when it is further down to the valence band. Figures 10(b), 10(d) and 10(f) are the diagrams of density of states for the Top, Hollow, and Bridge positions of Cu@graphene sample, respectively. It is found that they are tapered rather than following the V-shape of the graphene model. Because the conduction band passes through the Fermi level, the density of states is no longer zero. The values at the Top position, Hollow position, and Bridge position are 1.100 eV, 1.050 eV, and 1.100 eV, respectively.

It can be seen from Figure 10 that the density of states values at the Fermi level obtained for the above three models do not show significant differences. At the same time, the positions of the maximum density of states for these three samples are quite different. They are now located at the dense valence band below the Fermi level, with values of Top position at 28.370 eV, Hollow position at 27.701 eV, and Bridge position at 28.499 eV. Clearly the maximum density of states for these three models are basically the same. Compared with the maximum density of state value of the graphene (e.g., 8.551 eV), those values at the Top position, Hollow position, and Bridge position are

all slightly higher. This indicates that the density of states of the Cu(111)/graphene interface model is mainly contributed by copper electrons.

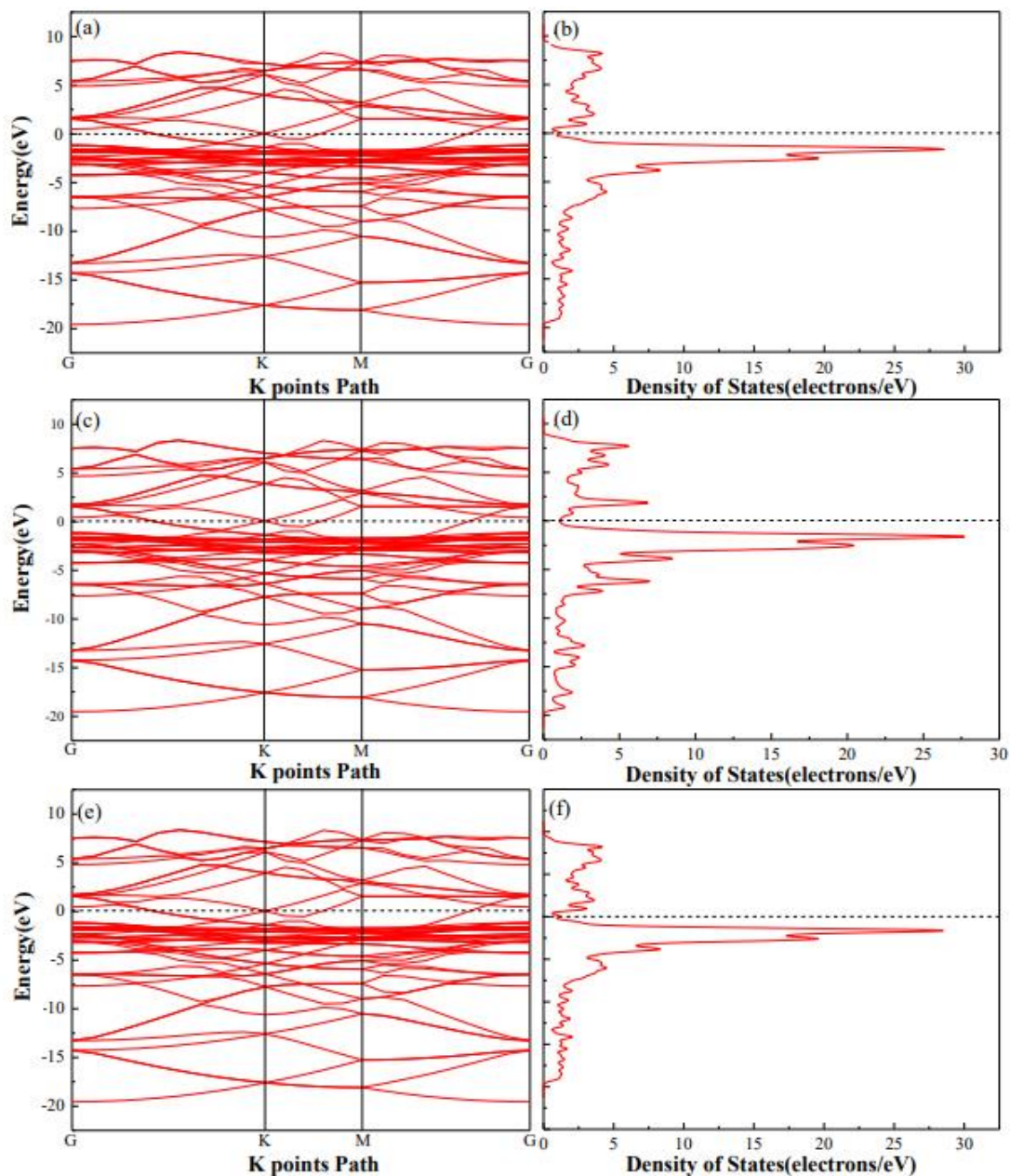


**Fig. 10.** Band structure diagrams and density of states diagram of the three adsorption models of Cu(111)/graphene. (a,d) Top, (b,e) Hollow, (c,f) Bridge.

The band structures and density of states calculation results of the Ni(111)/graphene interface model are shown in Figure 11. Figures 11(a), 11(c), and 11(e) are its energy band structure diagrams of Top position, Hollow position and Bridge position, respectively. Compared with the energy band structure diagram of graphene, the Fermi level of Ni(111)/graphene interface model is still at the intersection between the graphene  $\pi$  band and  $\pi^*$  band. Due to the existence of a layer of nickel atoms, the

conduction band is now crossing the Fermi level, but the forbidden band width is still zero. This shows that adding nickel into graphene does not change the zero bandgap of graphene. Whereas because nickel is a magnetic material, its band structure exhibits spin-up and spin-down phenomena, and accordingly the corresponding density of states also shows the same phenomenon. At the same time, the upper conduction band in the energy band diagram of the interface model is not dense. The lower valence band near the Fermi level is very dense, but it becomes loosen when it is further down to the valence band. Figures 11(b), 11(d) and 11(f) are the obtained diagram of densities of states for the Top, Hollow, and Bridge positions of the Ni(111)/graphene interface model, respectively. It is found that they are tapered rather than the V-shape of the graphene model. Because the conduction band of the Ni(111)/graphene passes through the Fermi level, its density of state value is not zero. These values of Ni(111)/graphene interface model are 0.984 eV for Top position spin up, -10.457 eV for Top position spin down, 0.962 eV for Hollow position spin up, and -9.939 eV for Hollow position spin down. The Bridge position spins up for 1.007 eV, and the Bridge position spins down for -10.487 eV. The values of the density of states at the Fermi level of the three models are quite similar. The maximum density of states is located at the places with dense valence bands below the Fermi level. Its values are Top position spin up 12.252 eV, Top position spin down -11.241 eV, Hollow position spin up 13.116 eV, and Hollow position spin down -11.098 eV. Compared with the maximum density of state of graphene (e.g., 8.551 eV), all those values for Ni@graphene are increased, but do not show significant differences. Therefore, it can be concluded that the densities of states of different models have little effects on the calculation of moduli of the graphene composite materials.

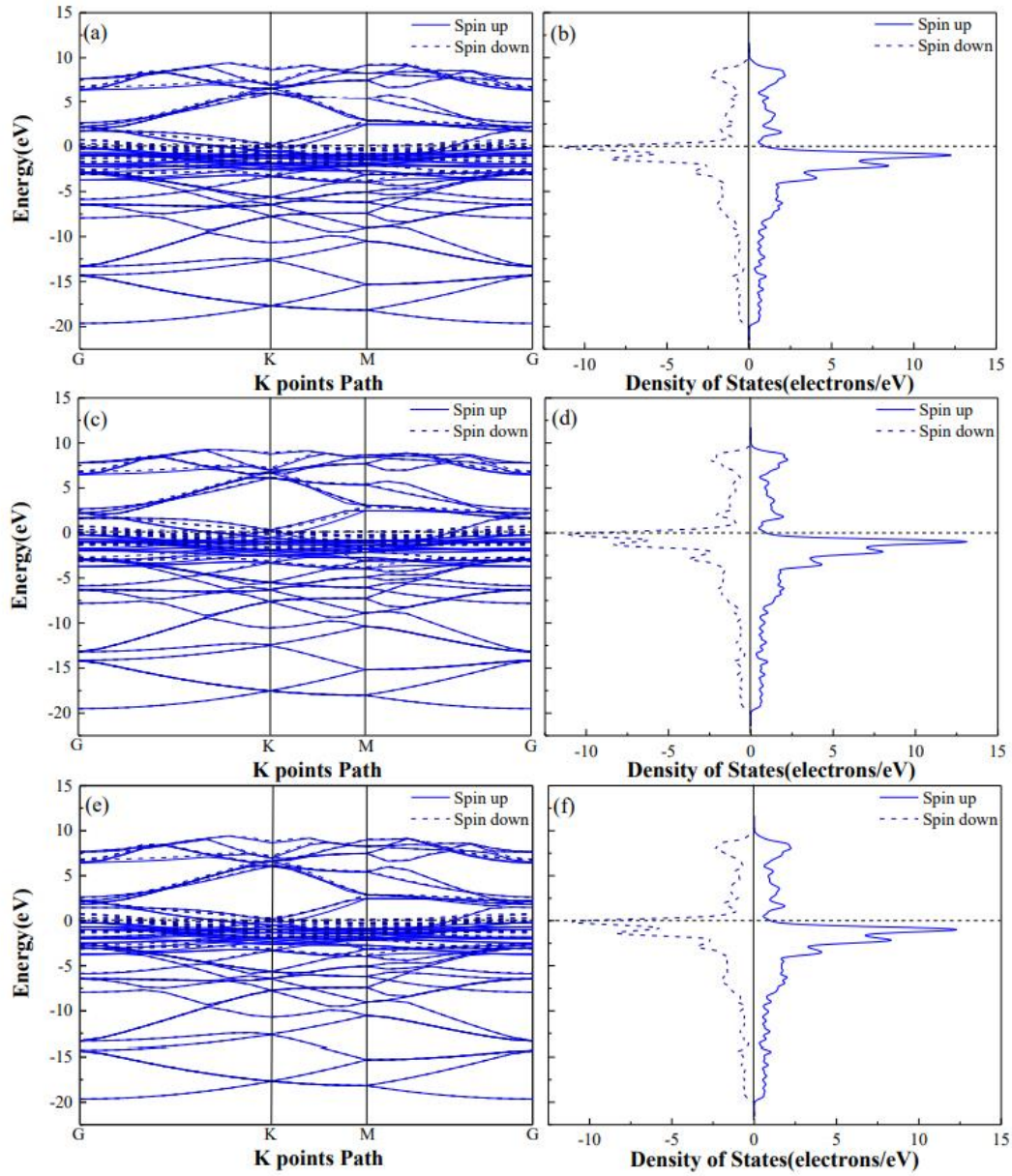


**Fig. 11.** Band structure diagrams and density of states diagram of the three adsorption models of Ni(111)/graphene, (a,d) Top, (b,e) Hollow, (c,f) Bridge.

For a two-dimensional material, its Young's modulus (in-plane) can be written as<sup>[49]</sup>:

$$Y^{2D} = \frac{C_{11}C_{22} - C_{12}^2}{C_{22}} \quad (5)$$

where  $C_{12}$  and  $C_{22}$  are independent elastic constants, which should satisfy  $C_{11} > 0$ ,  $C_{11} - C_{12} > 0$ ,  $C_{12} + 2C_{12} > 0$ <sup>[51]</sup>. We further calculated the elastic constants based on the relationship between strain and elastic potential energy when the model was deformed under elastic force<sup>[52]</sup>:

$$\frac{\Delta E}{V} = \frac{1}{2}(C_{11}\varepsilon_1\varepsilon_1 + C_{12}\varepsilon_1\varepsilon_2 + C_{12}\varepsilon_2\varepsilon_1 + C_{22}\varepsilon_2\varepsilon_2 + \frac{C_{11}-C_{12}}{2}\varepsilon_3) \quad (6)$$

where  $\Delta E$  is the elastic potential energy that deforms the model,  $V$  is the volume change of the model,  $\varepsilon_1 \sim \varepsilon_3$  are the strain components in each direction. The strain components are represented in the form of space vectors as  $\varepsilon_1=(0, \delta, 0)$ ,  $\varepsilon_2=(0, 0, \delta)$  and  $\varepsilon_3=(\delta, \delta, 0)$ , where  $-2\% \leq \delta \leq +2\%$  is the strain range. Finally,  $C_{11}$ ,  $C_{12}$  and  $C_{22}$  are obtained by Eq. (6) using the model and software.

The calculated moduli of graphene and metal-coated graphene based on the first principles calculations are listed in Table 1. According to Eq. (5), the calculated modulus of graphene is  $1100.35 \pm 0.003$  GPa, which is consistent with the experimental test result of 1060 GPa. The experimental results can be verified by the calculation results, and are also comparable with those reported in literature. For example, Andrew et al. [49] calculated the graphene's modulus to be 1053.5 GPa based on the local-density approximation (LDA) algorithm. Cho et al. [53] calculated using the Mori-Tanaka algorithm of graphene and obtained a modulus of 1153.00 GPa. Tsai et al. [54] used a molecular dynamics (MD) method and calculated the modulus of graphene to be 912.00 GPa. Compared with those reported in literature, the results obtained using the calculation models in this paper are quite similar. Compared with the experimentally obtained results of 1030 GPa and 980 GPa for the Cu@graphene and Ni@graphene, the calculation results are slightly higher, mainly because the defects in the samples were not considered when the models were built.

Tab.1. Calculation results of Young's modulus of graphene and metal@graphene

	method	$C_{11}$	$C_{22}$	$C_{12}$	$Y^{2D}$ (GPa)
graphene model	GGA-PBE	1130.00	1130.00	183.04	1100.35
graphene powder	experiment	-	-	-	1060
R.C. [49]	LDA	1091.9	1091.9	204.7	1053.5
Cho [53]	Mori-Tanak	-	-	-	1153.00
Tsai [54]	MD	977.91	978.19	254.46	912.00
Cu(111)/graphene	Top	1030.24	1030.24	190.22	1065.35
	Hollow	1036.26	1036.26	188.52	1070.56
	Bridge	1026.74	1026.74	201.36	1066.23
Ni(111)/graphene	Top	999.72	999.72	153.23	1023.21
	Hollow	1058.76	1058.76	168.25	1085.50
	Bridge	1030.87	1030.87	142.69	1050.62

The binding energy reflects the bonding strength between two different atoms. To compare the differences of bonding strengths between the two metals and graphene at different positions, we theoretically calculated their binding energy values. The interface binding energy formula<sup>[55]</sup> can be written as below:

$$E = E_{ab} - (E_a + E_b) \quad (7)$$

where  $E_{ab}$  represents the total energy of the adsorption model system, and  $E_a$  represents the formation energy of the metal atomic layer,  $E_b$  represents the formation energy of the graphene monolayer. We used an atom layer-thick metal film for theoretical calculation of the binding energy<sup>[56]</sup>. Although this might have the problem that the calculated binding energy is relatively small<sup>[57]</sup>, it should be suitable to compare bonding energy values of two metals with graphene in different positions. The obtained calculation results are listed in Table 2. The binding energies of the Top, Hollow and Bridge positions for the Cu(111)/graphene interface model are -1.51 eV, -1.54 eV and -1.54 eV, respectively. It can be concluded that the binding energies of the three different adsorption sites do not show apparent differences, indicating that the construction method does not affect the bonding of metal atoms and graphene. The binding strengths between the metal atom and the carbon atom are the same, and it is also the case for the center position of the metal atom and the carbon hexagon, as well as the metal atom and the carbon-carbon bond.

Our results can be supported by those reported in literature. For example, Jia et al.<sup>[58]</sup> used the first-principle method to calculate the adsorption binding energies of the Top, Center, and Bridge positions when a single copper atom was adsorbed on the graphene surface, and obtained values were -0.94 eV, -0.89 eV and -0.97 eV, respectively. They showed that the binding energies of these three adsorption sites did not show apparent differences, but due to the differences in single-atom adsorption and calculation accuracy, the binding energy was slightly smaller. Sidorenkov et al.<sup>[59]</sup> used the MD method to calculate the binding energy between Cu(111) and graphene and they obtained a value of 180 eV/Atom. Vanin et al.<sup>[60]</sup> used the vdW-DF algorithm and the LDA exchange correlation function to calculate the binding energy between Cu(111) and graphene, and obtained a value of 38 eV/Atom. Using different forms of exchange-related functionals and algorithms, the binding energy values between Cu(111) and graphene are quite different. Han et al.<sup>[57]</sup> further explained the detailed influences of different exchange-related functionals and different thicknesses of Cu(111) slab based on the calculated surface energies.

Table 2 lists the binding energies of the Top, Hollow and Bridge positions in the Ni(111)/graphene interface model, which are -4.02 eV, -4.00 eV and -3.75 eV, respectively. This reveals that the binding energies of the three different adsorption sites do not show significant differences. The binding energy results of the Ni(111)/graphene interface model and the Cu(111)/graphene interface model are slightly larger, indicating that the binding of nickel atoms to graphene is stronger than the binding of copper atoms to graphene. Zhang et al. <sup>[61]</sup> used the optB88-vdW algorithm to calculate the interface binding energies of two different construction cases (e.g., top-fcc and bridge-top) between Ni(111) surface and graphene. They obtained the values of -0.14 eV and -0.13 eV, which are similar to the results obtained from this study. Amaya et al. <sup>[62]</sup> used the VASP software and the GGA-PBE algorithm to calculate the interface binding energy of two different construction cases (e.g., fcc and hcp) between Ni(111) surface and graphene, and obtained the values of -3.81 eV and -3.81 eV. Clearly the numerical results of binding energy are slightly different due to differences in the calculation software, calculation methods, calculation parameters and calculation accuracy. However, our calculation results are in good agreements with those from the literature.

Tab.2. The calculation result of Binding Energy of metal@graphene

	model	graphene/eV	(111)/ eV	Binding Energy/ eV
Cu(111)/graphene	Top	-5405.75	-1676.78	-1.51
	Hollow	-5405.75	-1676.78	-1.54
	Bridge	-5405.75	-1676.78	-1.54
Ni(111)/ graphene	Top	-5405.75	-1368.61	-4.02
	Hollow	-5405.75	-1368.61	-4.00
	Bridge	-5405.75	-1368.61	-3.75

To study the bond formation and charge transfer between Cu and graphene, the differential charge densities were calculated for three interface models of Cu(111)/graphene, and the obtained results are shown in Fig. 12. Fig. 12(a) shows the differential charge density map of the Top position. The lateral charge around the C atom at the bottom is shown in a blue color, and the vertical charge is shown in a yellow one. The charge around the copper atom in the upper layer is shown in an orange-yellow color. Based on the Color Map, it can be seen that the blue area represents charge divergence, and the yellow area represents charge accumulation. These results indicate that carbon atoms lose electrical charges and copper atoms gain charges.

Fig. 12(b) shows the differential charge density diagram of the Hollow site, which



shows the differences of charge densities between the top site and the top site. Similar to the charge density diagram, the horizontal charge around the C atom at the bottom is shown in a blue color, and the vertical charge is shown in a yellow color. Different from the differential charge density diagram at the Top position, the charge around the copper atom in the upper layer is shown in a light yellow color. Based on the Color Map, the carbon atoms lose electrical charge and the copper atom gain charge.

Fig. 12(c) shows the differential charge density map of the Bridge position. Similarly, the lateral charge around the C atom is shown in a blue color, whereas the charge in a vertical direction is shown in a yellow color. The charge around the copper atoms in the upper layer is shown in an orange-yellow color, indicating that the carbon atoms lose charge and the copper atoms gain charge. These are consistent with the differential charge density map of the Top site.

It can be concluded that the interaction between adjacent carbon atoms in graphene is strong. When a layer of copper atoms is built on top of graphene, the charge density between these two carbon atoms that are originally bonded is decreased. At the same time, the charge density around the copper atom is increased, indicating that the charge is transferred from the C atom to the Cu atom, which is consistent with the previous calculation results from the energy band structure and density of states. Differential charge densities were calculated for three interface models of Ni(111)/graphene, and the results are shown in Fig.12(d) to 12(f). The results are similar to those of the Cu(111)/graphene.

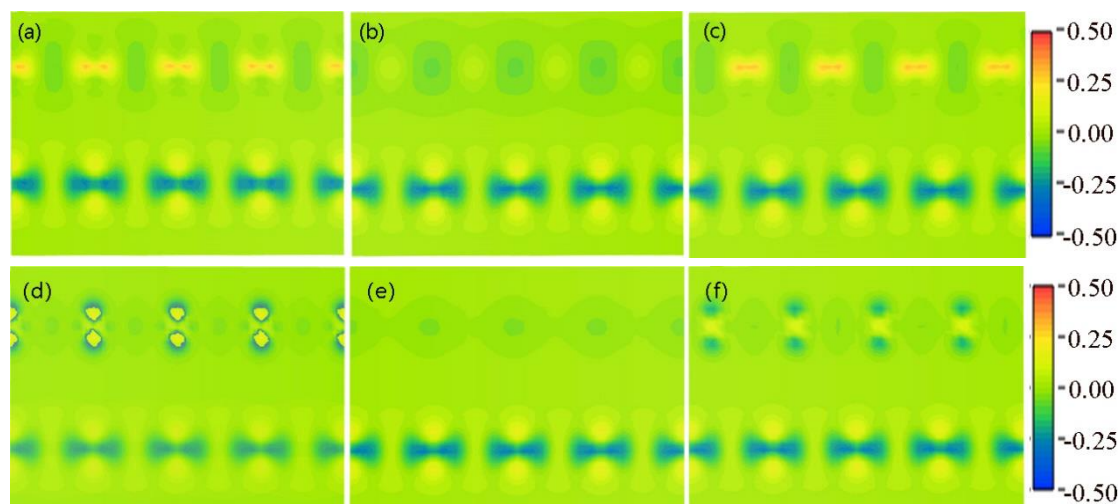


**Fig.12** The difference charge density map of Cu(111)/graphene models (a) Top; (b) Hollow; (c) Bridge; Ni(111)/graphene models (d) Top; (e) Hollow; (f) Bridge



## 4. Conclusions

Following conclusions can be obtained from this study:

- (1) Graphene powders and metal@graphene composite powders are obtained using the *in-situ* co-reduction method. Graphene shows a single atomic layer of tulle-like structure with a thickness of 1.1 nm. The thickness of Cu@graphene is ~3.0 nm, and the thickness of Ni@graphene is ~5.8 nm. The Young's moduli of graphene, Cu@graphene and Ni@graphene are 0.98 TPa, 1.03 TPa and 1.06 TPa. It shows that the mechanical properties of metal@graphene are as good as that of graphene.
- (2) The Young's moduli calculated using the first principles method are: graphene ( $1100.35 \pm 0.003$ ) GPa; Cu(111)/graphene ( $1066.23 \pm 0.003$ ) GPa; Ni(111)/graphene ( $1050.62 \pm 0.008$ ) GPa. The numerical results are generally similar to the measurement results.
- (3) The binding energy between metal and graphene is -1.54 eV for Cu(111)/graphene and -3.85 eV for Ni(111)/graphene. This shows that the binding between nickel atoms and graphene is stronger than the binding between copper atoms and graphene.
- (4) A charge transfer phenomenon is observed between carbon atoms and metal atoms, which enhances the bonding strengths of both C-C and metal bonds.

## Acknowledgement

The authors would like to acknowledge the financial supports from Key Research and Development Projects of Shaanxi Province (No. 2020ZDLGY12-06), Xi'an Science research project of China (No.2021XJZZ0042) and International Exchange Grant (IEC/NSFC/201078) through Royal Society and National Science Foundation of China (NSFC).

## Author Contributions

W.C. supported and supervised the project; Y.F. and X.L. supported and advised on the project; J.W., and Y.X. designed and performed the experiments; J.W. made the microstructure characterization and Y.X. made the phase structure; W.C., Q.Z. and Y.F. analyzed data and wrote the manuscript and all the authors modified and corrected the manuscript.

**Conflicts of Interest**

The authors declare no conflicts of interest.

## References

- [1] A.K. Geim, K.S. Novoselov, The rise of graphene, *Nature Materials* 6(3) (2007) 183-191.
- [2] C. Lee, X. Wei, J.W. Kysar, J. Hone, Measurement of the Elastic Properties and Intrinsic Strength of Monolayer Graphene, *Science* 321(5887) (2008) 385.
- [3] Y. Zhu, S. Murali, W. Cai, X. Li, J.W. Suk, J.R. Potts, R.S. Ruoff, ChemInform Abstract: Graphene and Graphene Oxide: Synthesis, Properties, and Applications, *ChemInform* 41(45) (2010).
- [4] M.M. Shokrieh, R. Rafiee, Prediction of Young's modulus of graphene sheets and carbon nanotubes using nanoscale continuum mechanics approach, *Materials & Design* 31(2) (2010) 790-795.
- [5] F. Liu, P. Ming, J. Li, Ab initio calculation of ideal strength and phonon instability of graphene under tension, *Physical Review B* 76(6) (2007) 064120.
- [6] M. Meo, M. Rossi, Prediction of Young's modulus of single wall carbon nanotubes by molecular-mechanics based finite element modelling, *Composites Science and Technology* 66(11) (2006) 1597-1605.
- [7] G.I. Giannopoulos, I.G. Kallivokas, Mechanical properties of graphene based nanocomposites incorporating a hybrid interphase, *Finite Elements in Analysis and Design* 90 (2014) 31-40.
- [8] K.N. Spanos, S.K. Georgantzinos, N.K. Anifantis, Mechanical properties of graphene nanocomposites: A multiscale finite element prediction, *Composite Structures* 132 (2015) 536-544.
- [9] J. Luo, S. Jiang, H. Zhang, J. Jiang, X. Liu, A novel non-enzymatic glucose sensor based on Cu nanoparticle modified graphene sheets electrode, *Analytica Chimica Acta* 709(2) (2012) 47-53.
- [10] C. Yu, Q. Su, R. Che, G. Du, B. Xu, One-step chemical vapor synthesis of Ni/graphene nanocomposites with excellent electromagnetic and electrocatalytic properties, *Synthetic Metals* 162(11-12) (2012) 968-973.
- [11] Z. Haiqing, Q. Caiyu, L. Zheng, Y. Huaichao, H. Lijun, L. Ji, Y. Haifang, G. Changzhi, S. Lianfeng, Thickness-dependent morphologies of gold on n-layer graphenes, *Journal of the American Chemical Society* 132(3) (2010) 944-6.
- [12] W. Hong, B. Hua, Y. Xu, Z. Yao, Z. Gu, G. Shi, Preparation of Gold Nanoparticle/Graphene Composites with Controlled Weight Contents and Their Application in Biosensors, *Journal of Physical Chemistry C* 114(4) (2010) 1822-1826.
- [13] H. Xiao, Z. Xiaozhu, W. Shixin, W. Yanyan, Q. Xiaoying, Z. Juan, B. Freddy, Z. Hua, Reduced graphene oxide-templated photochemical synthesis and in situ assembly of Au nanodots to orderly patterned Au nanodot chains, *Small* 6(4) (2010) 513-516.
- [14] H. Yaojuan, Z. Hua, W. Ping, Z. Hui, Z. Bo, C. Chenxin, Bimetallic Pt-Au nanocatalysts electrochemically deposited on graphene and their electrocatalytic characteristics towards oxygen reduction and methanol oxidation, *Physical Chemistry Chemical Physics* 13(9) (2011) 4083-4094.

- [15] W. Yan, Z. Yan, T. Bao, L. Xiang, Y. Su, Y. Duan, Preparation of Ni-reduced graphene oxide nanocomposites by Pd-activated electroless deposition and their magnetic properties, *Applied Surface Science* 258(22) (2012) 8603---8608.
- [16] M. Sun, J.P. Chou, Y. Zhao, Y. Jin, W. Tang, Weak C–HF–C hydrogen bonds make a big difference in graphane/fluorographane and fluorographane/fluorographane bilayers, *Physical Chemistry Chemical Physics* (41) (2017).
- [17] J. Mullen, K. Borysenko, E. Barry, Y. Semenov, M. Buongiorno Nardelli, J. Zavada, K. Kim, Effects of Electron-Phonon Interaction in Graphene: The First Principle Calculation, (2010).
- [18] W.G. Vandenberghe, M.V. Fischetti, Calculation of electron-phonon interaction strength from first principles in graphene and silicon, 2014 International Workshop on Computational Electronics (IWCE), 2014.
- [19] X. Ji, Y. Wang, Z. Yu, A first-principle investigation of double-side CVD catalyst metal/graphene contacts, *Physical Chemistry Chemical Physics* 16(24) (2014) 12327-12331.
- [20] S. Wang, J.-P. Chou, C. Ren, H. Tian, J. Yu, C. Sun, Y. Xu, M. Sun, Tunable Schottky barrier in graphene/graphene-like germanium carbide van der Waals heterostructure, *Scientific Reports* 9(1) (2019) 5208.
- [21] Y. Kim, J. Baek, S. Kim, S. Kim, S. Ryu, S. Jeon, S.M. Han, Radiation Resistant Vanadium-Graphene Nanolayered Composite, *Scientific Reports* 6(1) (2016) 24785.
- [22] R. Drost, S. Kezilebieke, M. M. Ervasti, S.K. Hämäläinen, F. Schulz, A. Harju, P. Liljeroth, Synthesis of Extended Atomically Perfect Zigzag Graphene - Boron Nitride Interfaces, *Scientific Reports* 5(1) (2015) 16741.
- [23] J. Jiang, P. Zhang, Y. Liu, H. Luo, A novel non-enzymatic glucose sensor based on a Cu-nanoparticle-modified graphene edge nanoelectrode, *Analytical methods* 9(14) (2017) 2205-2210.
- [24] L. Hu, X. Hu, X. Wu, C. Du, Y. Dai, J. Deng, Density functional calculation of transition metal adatom adsorption on graphene, *Physica B: Condensed Matter* 405(16) (2010) 3337-3341.
- [25] M. Sun, W. Tang, Q. Ren, S. Wang, JinYu, Y. Du, Y. Zhang, First-principles study of the alkali earth metal atoms adsorption on graphene, *Applied Surface Science* 356(NOV.30) (2015) 668-673.
- [26] Q. Zhou, Z. Fu, Y. Tang, H. Zhang, C. Wang, First-principle study of the transition-metal adatoms on B-doped vacancy-defected graphene, *Physica E: Low-dimensional Systems and Nanostructures* 60 (2014) 133-138.
- [27] Hao, Yitong, Sun, Minglei, Tang, Wencheng, Yu, Jin, Du, Yanhui, Electronic and magnetic behaviors of graphene with 5d series transition metal atom substitutions: A first-principles study, *Physica, E. Low-dimensional systems & nanostructures* (2016).
- [28] M. Chi, Y.-P. Zhao, Adsorption of formaldehyde molecule on the intrinsic and Al-doped graphene: A first principle study, *Computational Materials Science* 46(4) (2009) 1085-1090.
- [29] M. Jiang, W. Zhang, K. Zhao, F. Guan, Y. Wang, Investigations on the electronic structure and optical properties of (Ga,N,Ga-N) doped graphene by first-

principle calculations, *International Journal of Modern Physics B* (2021).

[30] F.W. Low, W. Chin, C.w. Lai, S.B. Abd Hamid, A. Hamid, Facile Synthesis of High Quality Graphene Oxide from Graphite Flakes Using Improved Hummer's Technique, *Journal of Nanoscience and Nanotechnology* 15 (2015) 1-5.

[31] C. Chen, Y.-C. Chen, Y.-T. Hong, T.-W. Lee, J.-F. Huang, Facile fabrication of ascorbic acid reduced graphene oxide-modified electrodes toward electroanalytical determination of sulfamethoxazole in aqueous environments, *Chemical Engineering Journal* 352 (2018) 188-197.

[32] Yuanlin, Xue, Wenge, Chen, Jiaojiao, Wang, Longlong, Dong, Qian, Zhao, Formation Mechanism and Cohesive Energy Analysis of Metal-Coated Graphene Nanocomposites Using In-Situ Co-Reduction Method, *Materials (Basel, Switzerland)* (2018).

[33] B.V. Derjaguin, V.M. Muller, Y.P. Toporov, Effect of contact deformations on the adhesion of particles, *Progress in Surface Science* 45(1) (1994) 131-143.

[34] Alvarez, Santiago, A cartography of the van der Waals territories, *Dalton Transactions* 42(24) (2013) 8617.

[35] H.K. Neupane, N.P. Adhikari, Structure, electronic and magnetic properties of 2D Graphene-Molybdenum diSulphide (G-MoS<sub>2</sub>) Heterostructure (HS) with vacancy defects at Mo sites, *Computational Condensed Matter* 24 (2020) e00489.

[36] J.C. Meyer, A.K. Geim, M.I. Katsnelson, K.S. Novoselov, T.J. Booth, S. Roth, The structure of suspended graphene sheets, *Nature* 446(7131) (2007) 60-63.

[37] D. Kuang, L. Xu, L. Liu, W. Hu, Y. Wu, Graphene–nickel composites, *Applied Surface Science* 273 (2013) 484-490.

[38] Y. Hu, J. Jin, P. Wu, H. Zhang, C. Cai, Graphene–gold nanostructure composites fabricated by electrodeposition and their electrocatalytic activity toward the oxygen reduction and glucose oxidation, *Electrochimica Acta* 56(1) (2010) 491-500.

[39] X. Guo, C. Hao, G. Jin, H.-Y. Zhu, X.-Y. Guo, Copper Nanoparticles on Graphene Support: An Efficient Photocatalyst for Coupling of Nitroaromatics in Visible Light, *Angewandte Chemie International Edition* 53(7) (2014) 1973-1977.

[40] Y. Cao, Q. Su, R. Che, G. Du, B. Xu, One-step chemical vapor synthesis of Ni/graphene nanocomposites with excellent electromagnetic and electrocatalytic properties, *Synthetic Metals* 162(11) (2012) 968-973.

[41] G. Jiaqiang, W. Yating, L. Lei, S. Bin, H. Wenbin, Crystallization temperature of amorphous electroless nickel–phosphorus alloys, *Materials Letters* 59(13) (2005) 1665-1669.

[42] A.C. Ferrari, Raman spectroscopy of graphene and graphite: Disorder, electron–phonon coupling, doping and nonadiabatic effects, *Solid State Communications* 143(1) (2007) 47-57.

[43] L.M. Malard, M.A. Pimenta, G. Dresselhaus, M.S. Dresselhaus, Raman spectroscopy in graphene, *Physics Reports* 473(5) (2009) 51-87.

[44] K.N. Kudin, B. Ozbas, H.C. Schniepp, R.K. Prud'homme, I.A. Aksay, R. Car, Raman Spectra of Graphite Oxide and Functionalized Graphene Sheets, *Nano Letters* 8(1) (2008) 36-41.

[45] L.-l. Dong, W.-g. Chen, N. Deng, C.-h. Zheng, A novel fabrication of

graphene by chemical reaction with a green reductant, *Chemical Engineering Journal* 306 (2016) 754-762.

[46] Y. Kim, Magneto-Raman spectroscopy of graphene and graphite: Probing electronic structure and electron-phonon interaction, The Florida State University., 2012.

[47] P. Nemes-Incze, Z. Osváth, K. Kamarás, L.P. Biró, Anomalies in thickness measurements of graphene and few layer graphite crystals by tapping mode atomic force microscopy, *Carbon* 46(11) (2008) 1435-1442.

[48] Y. Yao, L. Ren, S. Gao, S. Li, Histogram method for reliable thickness measurements of graphene films using atomic force microscopy (AFM), *Journal of Materials Science & Technology* 33(8) (2017) 815-820.

[49] R., C., Andrew, R., E., Mapasha, A., M., Ukpong, N., Mechanical properties of graphene and boronitrene, *Physical Review B* 85(12) (2012) 125428-125428.

[50] Z. Xu, M.J. Buehler, Interface structure and mechanics between graphene and metal substrates: a first-principles study, *Journal of Physics: Condensed Matter* 22(48) (2010) 485301.

[51] Yu Jin , first-principles calculations, Science Press (2016).

[52] V. Wang, N. Xu, J.C. Liu, G. Tang, W.T. Geng, VASPKIT: A user-friendly interface facilitating high-throughput computing and analysis using VASP code, *Computer Physics Communications* (2021) 108033.

[53] J. Cho, J.J. Luo, I.M. Daniel, Mechanical characterization of graphite/epoxy nanocomposites by multi-scale analysis, *Composites Science & Technology* 67(11-12) (2007) 2399-2407.

[54] J.L. Tsai, J.F. Tu, Characterizing mechanical properties of graphite using molecular dynamics simulation, *Materials & Design* 31(1) (2010) 194-199.

[55] Kiefer, B., Serov, A., Kabir, S., Artyushkova, K., Atanassov, P., Binding energy shifts for nitrogen-containing graphene-based electrocatalysts - experiments and DFT calculations, *Surface and Interface Analysis: SIA: An International Journal Devoted to the Development and Application of Techniques for the Analysis of Surfaces, Interfaces and Thin Films* 48(5) (2016) 293-300.

[56] J. Hernández, E.C. Anot, M. Cruz, M.G. Melchor, G.H. Coccoletzi, First principles studies of the graphene-phenol interactions, *Journal of Molecular Modeling* 18(8) (2012) 3857-3866.

[57] Y. Han, K.C. Lai, A. Lii-Rosales, M.C. Tringides, J.W. Evans, P.A. Thiela, Surface energies, adhesion energies, and exfoliation energies relevant to copper-graphene and copper-graphite systems, *Surface Science* 685(JUL.) (2019) 48-58.

[58] C. Jia, H. Yu, structures and thermodynamical stabilities of single-atom adsorbed cu / graphene systems, *Journal of Natural Science of Heilongjiang University* (02) (2015) 77-81+145.

[59] A.V. Sidorenkov, S.V. Kolesnikov, A.M. Saletsky, Molecular dynamics simulation of graphene on Cu(111) with different Lennard-Jones parameters, *European Physical Journal B* 89(10) (2016) 220.

[60] M. Vanin, J.J. Mortensen, A.K. Kelkkanen, J.M. Garcia-Lastra, K.S. Thygesen, K.W. Jacobsen, Graphene on metals: A van der Waals density functional

study, Physical review 81(8) (2010) p.081408.1-081408.4.

[61] W.-B. Zhang, C. Chen, P.-Y. Tang, First-principles study for stability and binding mechanism of graphene/Ni(111) interface: Role of vdW interaction, The Journal of Chemical Physics 141(4) (2014) 044708.

[62] S. Amaya-Roncancio, A. Blanco, D.H. Linares, K. Sapag, DFT Study of Hydrogen Adsorption on Ni/graphene, Applied Surface Science 447 (2018).